Geochemistry, Geophysics, Geosystems

Water-rich bending faults at the Middle America Trench

Samer Naif[1], Kerry Key[1], Steven Constable[1], and Rob L. Evans[2]

[1]Institute of Geophysics and Planetary Physics, Scripps Institution of Oceanography, University of California San Diego, La Jolla, California, USA, [2]Department of Geology and Geophysics, Woods Hole Oceanographic Institution, Woods Hole, Massachusetts, USA

Abstract The portion of the Central American margin that encompasses Nicaragua is considered to represent an end-member system where multiple lines of evidence point to a substantial flux of subducted fluids. The seafloor spreading fabric of the incoming Cocos plate is oriented parallel to the trench such that flexural bending at the outer rise optimally reactivates a dense network of normal faults that extend several kilometers into the upper mantle. Bending faults are thought to provide fluid pathways that lead to serpentinization of the upper mantle. While geophysical anomalies detected beneath the outer rise have been interpreted as broad crustal and upper mantle hydration, no observational evidence exists to confirm that bending faults behave as fluid pathways. Here we use seafloor electromagnetic data collected across the Middle America Trench (MAT) offshore of Nicaragua to create a comprehensive electrical resistivity image that illuminates the infiltration of seawater along bending faults. We quantify porosity from the resistivity with Archie's law and find that our estimates for the abyssal plain oceanic crust are in good agreement with independent observations. As the Cocos crust traverses the outer rise, the porosity of the dikes and gabbros progressively increase from 2.7% and 0.7% to 4.8% and 1.7%, peaking within 20 km of the trench axis. We conclude that the intrusive crust subducts twice as much pore water as previously thought, significantly raising the flux of fluid to the seismogenic zone and the mantle wedge.

1. Introduction

Subduction of hydrated oceanic lithosphere is the primary process by which water is transported to the interior of the Earth [*Thompson and Connolly*, 1992; *Hirschmann*, 2006]. The magnitude of water subducted modulates many fundamental tectonic processes, including seismic coupling at the megathrust plate interface [*Scholz*, 1998; *Saffer and Tobin*, 2011] and arc magma genesis [*Gaetani and Grove*, 1998]. Quantifying the flux of water transported by oceanic plates and the distribution of fluids released during subduction is critical to understanding the pattern of seismic coupling at the plate interface as well as chemical and volatile cycling between the solid and fluid Earth.

Subducting tectonic plates transport interstitial and mineral-bound water that is partitioned into sediment, crust, and upper mantle reservoirs. Pore water trapped in benthic sediment can account for close to half of the total influx depending on the fraction that is underthrust into the margin with the subducting slab [*Plank and Langmuir*, 1998; *Jarrard*, 2003]. The magnitude of volatiles in the upper extrusive oceanic crust tend to increase with age, where older extrusive crust contains relatively more mineral-bound and less interstitial water than younger crust [*Carlson and Herrick*, 1990; *Staudigel*, 2014]. In contrast, the volatile content of the intrusive oceanic crust is generally assumed to remain constant with age, although in situ observational constraints on the hydration state of the lower crust are limited. Given these assumptions, the combined magnitude of extrusive and intrusive crustal water subducted is estimated to vary by only 3% between 5 and 145 million year old (Ma) plate [*Jarrard*, 2003]. This suggests that the flux of crustal water is fairly uniform at all convergent margins, with regional differences dictated by sediment heterogeneity.

Mineral-bound water in the oceanic upper mantle could rival or significantly exceed the combined flux of crustal and sedimentary sources in the global subduction zone water budget [*Ulmer and Trommsdorff*, 1995; *Rüpke et al.*, 2004], but the degree of mantle hydration is poorly constrained [*Hacker*, 2008]. The upper mantle of an oceanic plate formed at a fast spreading ridge is expected to be relatively dry, which is consistent with observations of electrically resistive oceanic lithosphere away from convergence zones [*Cox et al.*, 1986; *Evans et al.*, 1994; *Key et al.*, 2013; *Baba et al.*, 2013]. Near the trench, flexural bending at the trench-
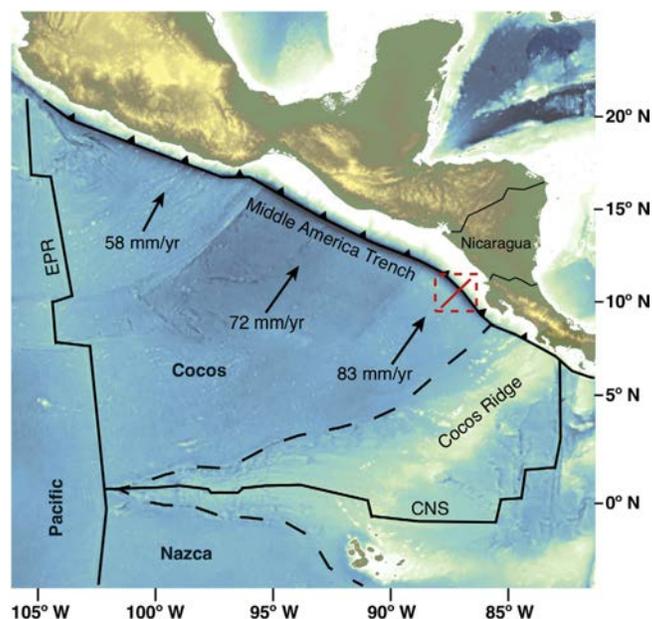
Figure 1. Regional tectonic map. The Cocos oceanic plate subducts at a rate that increases from 40 mm/yr in the northwest to 90 mm/yr in the southeast [*DeMets et al.*, 2010]. The black dashed line marks the boundary that separates the Cocos crustal origin between the East Pacific Rise (EPR) and the Cocos-Nazca spreading center (CNS). The survey profile (boxed) is located on EPR-sourced crust and crosses the MAT off Nicaragua.

outer rise generates Moho crossing normal faults that may provide a permeable pathway for seawater to percolate into the mantle [*Peacock*, 2001; *Ranero et al.*, 2003; *Faccenda et al.*, 2009]. At temperatures below 450°C, the addition of water to mantle peridotite triggers a series of alteration reactions that consume H_2O and form hydrous serpentinite minerals [*Moody*, 1976].

To date, regional active-source seismic studies at the outer rise provide the only in situ estimates of mantle hydration [*Ranero and Sallarès*, 2004; *Contreras-Reyes et al.*, 2007; *Ivandic et al.*, 2008; *van Avendonk et al.*, 2011]. By comparison, fluid fluxes in the sediment and extrusive crust are better constrained by a relative abundance of observations, but the large interstudy variability of H_2O estimated to subduct suggests important uncertainties remain [*Kastner et al.*, 2014].

2. The Middle America Trench

The Central American landmass is an uplifted block on the western portion of the Caribbean plate. It includes the Central America Volcanic Arc (CAVA), formed by the ongoing subduction of the Cocos oceanic plate beneath the western edge of the Caribbean plate [*Mann et al.*, 2007]. The border between the two plates is marked by the Middle America Trench (MAT).

The Nicaraguan portion of the CAVA is unique in that it has been found to be unusually rich in fluids. Lava samples from its arc volcanoes contain the strongest geochemical signatures found to date, linking the erupting material to a large flux of fluids and sediment derived from the subducting slab [*Morris et al.*, 1990; *Patino et al.*, 2000]. The subducting slab has fed the mantle wedge with a relatively steady state supply of sediment for the last 20 Ma [*Plank et al.*, 2002].

Beneath the Nicaraguan volcanic arc, seismic studies detect high Vp/Vs ratios, reduced velocities, and high attenuation in the mantle wedge that are all consistent with a large flux of fluids and/or magma [*Rychert et al.*, 2008; *Syracuse et al.*, 2008; *Dinc et al.*, 2011]. Additionally, anomalies at depths coincident with the subducting slab suggest that the downgoing oceanic crust and the uppermost mantle are highly hydrated [*Abers et al.*, 2003; *Syracuse et al.*, 2008].

Figure 1 shows the tectonic setting of Central America. The Cocos crust is born out of two independent mid-ocean ridges: the north-south trending East Pacific Rise (EPR) and the east-west trending Cocos-Nazca Spreading center (CNS). The boundary between the two runs southwest-northeast and meets the MAT off the Nicoya Peninsula [*Barckhausen et al.*, 2001].

The distinction between crustal origin is important because the thickness, seismic velocity, and heat flow signatures of the EPR and CNS crust are starkly different. The EPR crust emits anomalously low heat flux, while the CNS crust shows typical heat flux for its age [*Fisher et al.*, 2003a; *Hutnak et al.*, 2008]. The EPR crust is also thin (5.5 km) and seismically fast relative to the 8–11 km thick CNS crust [*Ivandic et al.*, 2008; *van Avendonk et al.*, 2011].

Offshore of Nicaragua, the seafloor spreading fabric and thus the remnant abyssal hill faults of the incoming EPR-sourced Cocos plate are oriented parallel to the trench axis. The plate begins to bend as it dives into the MAT, forming an outer rise flexural bulge that reactivates remnant faults to produce what are often referred to as bending faults. A seismic reflection survey off southern Nicaragua imaged bending faults extending several kilometers into the upper mantle [*Ranero et al.*, 2003].

Multibeam bathymetric maps show the associated scarps reaching several hundred meters of vertical offset [*Weinrebe and Ranero*, 2012]. The thin sediment cover indicates that the scarps likely expose basaltic basement to seawater. Outcropping basement highs on the EPR-Cocos plate have been linked to recharge and discharge of fluids, fueling hydrothermal circulation in the relatively permeable upper oceanic crust [*Fisher et al.*, 2003b; *Hutnak et al.*, 2008]. Fluid circulation through basement outcrops in tandem with the possibility that faults generate wide damage zones suggests that exposed seafloor faults may provide permeable fluid pathways to depth [*Peacock*, 2001]. This hypothesis is supported by a numerical model that shows subhydrostatic pressure gradients arise from outer rise extensional stresses, allowing seawater to percolate to upper mantle depths [*Faccenda et al.*, 2009].

If bending faults promote the migration of seawater to Moho depths at the outer rise, a late-stage of serpentinization will ensue. During subduction, serpentinite phases become unstable as they are subjected to higher pressures and temperatures, eventually undergoing dehydration reactions that supply a substantial flux of H_2O to the overlying mantle wedge [*Hacker*, 2008; *van Keken et al.*, 2011]. Since water lowers the solidus of mantle minerals [*Kushiro et al.*, 1968; *Gaetani and Grove*, 1998], outer rise serpentinization may promote additional magmatic production that ultimately increases volcanic activity in the arc. At subsolidus temperatures, such water may also lead to serpentinization of the overriding mantle, changing the frictional properties of the plate interface and thus the behavior of the megathrust seismogenic zone [*Beroza and Ide*, 2011; *Kaproth and Marone*, 2013].

Serpentinite is significantly less dense and as such has a lower seismic velocity than its parent rock [*Carlson and Miller*, 2003]. Wide-angle seismic data collected along the MAT detect velocity reductions in the upper mantle, indicating that some amount of serpentinized minerals are likely present. Estimates range from 15 to 40% serpentinization in the top 4–12 km below the Moho [*Ivandic et al.*, 2008; *van Avendonk et al.*, 2011; *Ivandic et al.*, 2010]. Naturally, observations of hydration at the Cocos outer rise have been linked to those of a fluid-rich mantle wedge [*Rüpke et al.*, 2002].

Due to the large bending moment, the oceanic lithosphere experiences extensional stresses that exceed its elastic yield strength at the trench-outer rise [*Levitt and Sandwell*, 1995; *Garcia et al.*, 2015], leading to brittle deformation in the crust and uppermost mantle. This likely has a significant effect on porosity, which may be concentrated in the damage zones surrounding bending faults. Seismic data have difficulty discriminating between fracture porosity and hydration, limiting the reliability of inferences for the oceanic crust (see discussion in *Ivandic et al.* [2008]). Mantle hydration is better constrained since the higher lithostatic pressures relative to the crust suggest that fracture porosity may be less of a concern below the Moho. Velocities consistent with serpentinization and evidence for fracture induced seismic anisotropy have been seen in the upper mantle in this region (D. Lizarralde, personal communication, 2015). Since existing estimates ignore fracture porosity, the extent of serpentinization inferred from seismic data is an upper bound. Electrical resistivity measurements offer an independent tool to help further constrain the nature of fluid circulation through the crust and into the mantle.

3. Marine CSEM Survey

In order to investigate subseafloor fluid migration and plate hydration, we collected controlled-source electromagnetic (CSEM) data to image electrical resistivity along a 220 km profile offshore of Nicaragua. Our survey—the Serpentinite, Extension, and Regional Porosity Experiment across the Nicaragua Trench (SERPENT)—spans the abyssal plain and trench-outer rise of the Cocos plate and the fore-arc slope of the Caribbean plate, shown in Figure 2. To date, this is the only marine CSEM data set collected at a subduction zone. Previous work by *Key et al.* [2012] used 1-D inversion to analyze the data. Here we employ recently developed 2-D inversion tools [*Key and Ovall*, 2011; *Key*, 2012] to model the data.

The CSEM method uses electromagnetic induction to map crustal resistivity variations, providing a powerful tool that can image fluid pathways and quantify porosity. The electrical resistivity of the crust, to first order,
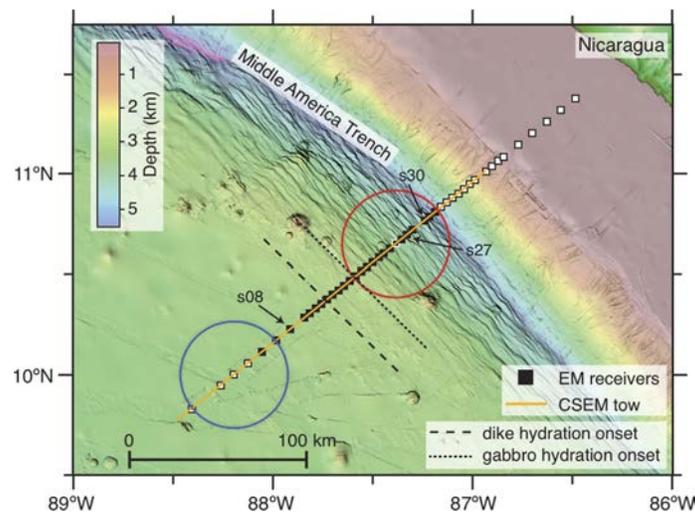
Figure 2. Map of the electromagnetic survey. The faulted seafloor fabric is clearly seen in the high-resolution bathymetric map. Solid black squares show the location of ocean bottom electromagnetic receivers whose data we consider here. The black square outlined in white is a LEM collocated with a standard receiver. Data from white squares outlined in black were excluded from modeling. The orange line shows the CSEM transmitter towpath and the blue and red circles are the LEM anisotropy tows. Data from sites s08 and s27 are shown in Figure 3. The black dashed line and black dotted line represent the location where our data observe the onset of hydration in the layer of dikes and gabbros at 80 km and 60 km seaward of the trench, respectively.

is dependent on porosity and the temperature and salinity of pore fluids [*Evans*, 1994]. Since saline water is up to six orders of magnitude less resistive than crystalline rock [*Quist and Marshall*, 1968], slight variations in pore fluid content will change bulk resistivity above the detection threshold of our broadband electromagnetic instruments [*Constable*, 2013]. Porosity is then estimated from resistivity by applying two-phase mixing models given assumptions about pore geometry and interconnection [*Becker et al.*, 1982; *Becker*, 1985].

Our instruments continuously record horizontal electric and magnetic field time series in two orthogonal directions. While it is possible to utilize naturally occurring electromagnetic fields to image electrical resistivity with the passive magnetotelluric (MT) method, attenuation of the high-frequency MT source field by the conductive ocean limits the ability of marine MT data to constrain shallow structure; previous marine MT results at the MAT resolve upper mantle electrical structure at depths corresponding to the lithosphere-asthenosphere boundary [*Worzewski et al.*, 2010; *Naif et al.*, 2013].

Considering that our primary objective is to image the crust, we augment the low-frequency MT data with CSEM data collected at higher frequencies. Acquiring CSEM data entails deep-towing an electric dipole antenna close to the seabed so that the transmitted energy couples to the seafloor, allowing it to propagate through the resistive oceanic crust. An array of receivers is used to measure the attenuation of this propagating energy, which depends on the seafloor electrical resistivity structure [*Cox et al.*, 1986; *Constable and Cox*, 1996].

We deep-towed the Scripps Undersea Electromagnetic Source Instrument (SUESI) approximately 100 m above the seafloor while it output 300 amps of alternating current from the dipole of a 250 m antenna. We used a complex binary waveform with a 4 s fundamental period to ensure a wide frequency spectrum suitable for constraining crustal structure [*Myer et al.*, 2011]. The transmissions were recorded by an array of 44 seafloor EM receivers sampling at 62.5 Hz. The standard receiver configuration had electrodes on the end of 10 m dipoles and induction coil magnetometers. We also deployed two pairs of long-wire electromagnetic (LEM) instruments that recorded the horizontal electric fields with 200 m electrode separation. The long electrode antenna reduces the electric field noise floor by one to two orders of magnitude compared with a standard receiver, significantly improving the data quality. Additional details concerning the survey design and instrumentation are described in *Key et al.* [2012]. Our analysis here considers CSEM data from one LEM and 26 standard receivers deployed along a 120 km segment of the incoming oceanic plate. Data from receivers located on the fore arc are being assessed independently (S. Naif et al., in preparation).

3.1. Data Processing

To obtain CSEM response functions, we transform the time series data into the frequency domain and normalize by the transmitter dipole moment to get Fourier coefficients for 4 s time-windows (the length of a single waveform) [*Myer et al.*, 2011]. We stack the resulting Fourier coefficients into 120 s intervals to increase the signal-to-noise ratio (SNR). Obvious outliers were discarded prior to stacking. The remaining
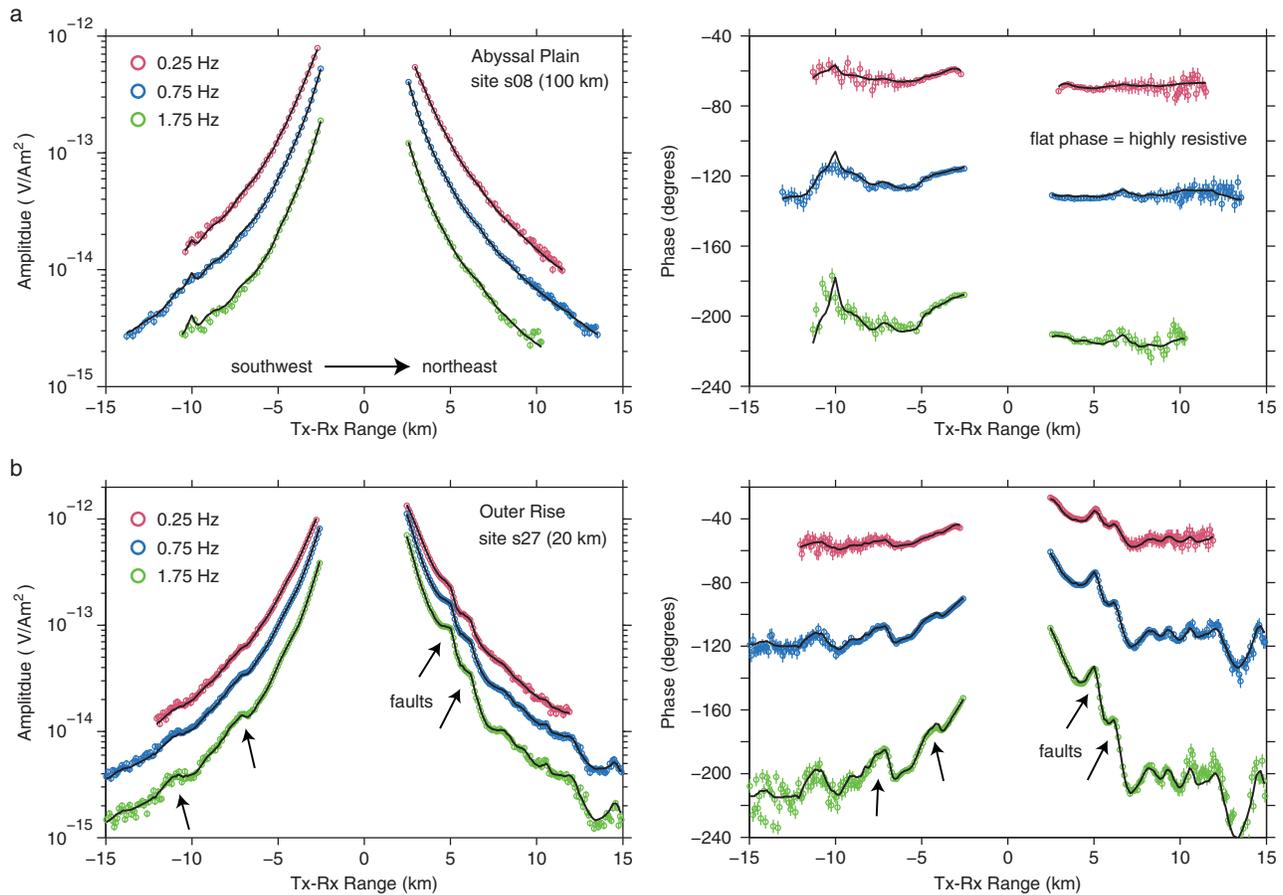
Figure 3. CSEM amplitude and phase data of the inline electric field at 0.25, 0.75, and 1.75 Hz from (a) site s08 on the landward edge of the abyssal plain and (b) site s27 on the heavily faulted outer rise, 20 km from the trench axis. Vertical bars are data uncertainties. The 2-D model responses (black lines) fit the structure of the data significantly better than previous 1-D model responses in *Key et al.* [2012].

data were stacked with a robust algorithm that iteratively flagged and removed data with residuals greater than three times the median absolute deviation until convergence.

The remaining high SNR data were rotated to the strike of the survey transect. We modeled the inline electric field responses (amplitude and phase) at the first, third, and seventh waveform harmonics (0.25, 0.75, and 1.75 Hz), where most of the waveform energy is concentrated. Inverting multiple frequencies of data significantly improves the model resolution and sensitivity compared with single frequency inversions [*Key*, 2009]. We limited the data to the electric field component because magnetic field data are susceptible to noise associated with instrument shaking and using both electric and magnetic field data adds redundant constraints [*Key*, 2009]. We used the transverse magnetic field data for site s30 (location shown in Figure 2) since it had a malfunctioning electrode but functional magnetometers.

We discarded all data with transmitter-receiver ranges of less than 2 km since navigation uncertainties are proportionally large at short ranges and can produce significant modeling errors. The short range data are mostly sensing the conductive sediment layer and so do not reduce our sensitivity to structure at crustal depths. Stacked data with SNR of less than two were also discarded. After filtering, we applied a 2% error floor to the remaining 25,864 data points deemed suitable for inversion. Example responses from two receivers are shown in Figure 3. Site s08 was deployed over smooth unfaulted seafloor (see Figure 2). The data reflect this, showing smoothly decaying amplitudes and flat phases with increasing source-receiver offset. The flat phase indicates the presence of a highly resistive basement. Site s27, by contrast, was deployed over heavily faulted seafloor in the outer rise. As a result of reduced sediment thickness from erosion, the amplitudes and phases noticeably increase as SUESI traverses fault scarps. Also note the decreasing trend in phase with increasing source-receiver offset, which indicates a relatively less resistive basement.
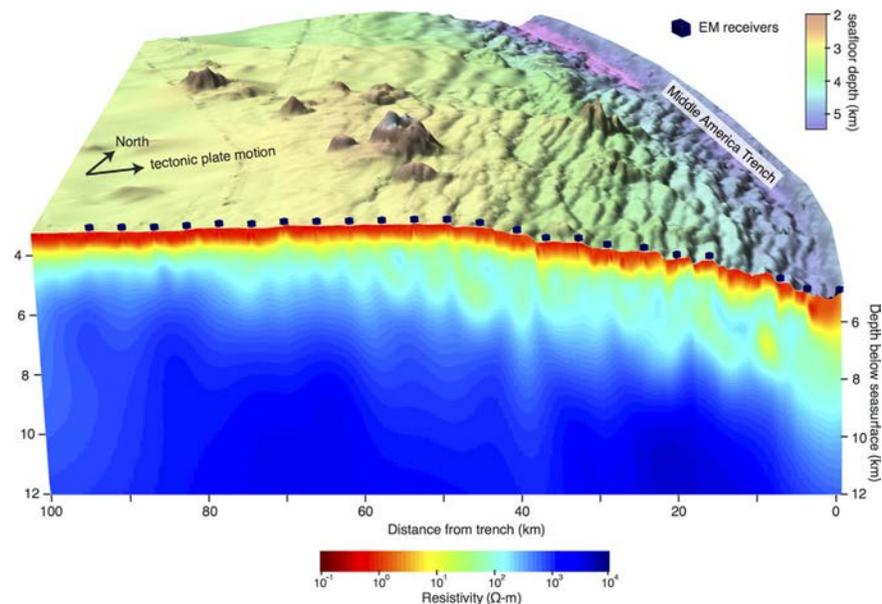
Figure 4. The electrical structure of the incoming Cocos plate from nonlinear inversion of deep-towed CSEM data. The vertical cross section shows the electrical resistivity structure and the stitched top plot shows seafloor bathymetry. The dark blue cubes show the location of EM receivers. The region of the seafloor marked by steeply dipping bathymetric relief correlates with subvertical conductive channels, which we interpret as evidence for the migration of seawater along bending faults.

The data at site s27 exemplify the importance of accurately incorporating seafloor relief in the model domain. We utilized the bathymetry derived from SUESI to finely discretize our parameter mesh. SUESI was equipped with an altimeter and depth pressure gauge that combine to map seafloor depth. The proximity of SUESI to the seafloor coupled with the large sampling rate and high operating frequency of the altimeter and depth pressure gauge yield submeter accuracy and along-track resolution, which is at least one order of magnitude better than multibeam bathymetry data in deep oceans.

3.2. 2-D Inversion Results

We used an open-source nonlinear regularized inversion scheme that employs an adaptive finite element solver to compute a two-dimensional isotropic resistivity model from the multifrequency CSEM responses [*Key and Ovall*, 2011; *Key*, 2012]. The model mesh was discretized with 27.5k parameters using rectangular elements. The inversion ran for a total of 16 h on 320 processing cores (2.6 GHz Intel Xeon E5) and converged after 15 iterations. Figure 4 shows the final converged electrical resistivity model, which fits the data to a root mean square (RMS) misfit of 1.0 relative to the 2% error floor. The inversion of the high-frequency CSEM data captures the electrical structure of the Cocos crust with significantly higher resolution than previous efforts with marine MT data [*Worzewski et al.*, 2010; *Naif et al.*, 2013]. The model residuals, including a breakdown of the data misfit, are shown in the supporting information.

Our model depicts spatially evolving electrical resistivity that correlates with the location and intensity of outer rise bending faults. Beyond 60 km seaward of the trench, both the bathymetry and resistivity are relatively one-dimensional. The electrical structure reflects compositionally distinct layers; a veneer of conductive high porosity sediment is underlain by an increasingly resistive and less porous crust and upper mantle. At the onset of dense faulting approximately 60 km from the trench, a heterogeneous electrical structure emerges. Seafloor fault scarps correlate with subvertical conductive channels that extend into the lower crust (Figure 5b). Because these conductive channels occur in step with normal faults and a porosity increase is the simplest explanation for the enhanced conductivity, we infer that seawater penetrates into the crust along fault damage zones. Fluidized faults can also account for the fault-parallel electrical anisotropy shown in Figure 5a, which was previously detected at the outer rise [*Key et al.*, 2012]. As the plate approaches the trench axis, the channels deepen and become more conductive, suggesting that additional fluids percolate to greater depths as the fault throw grows and the crust is further damaged.
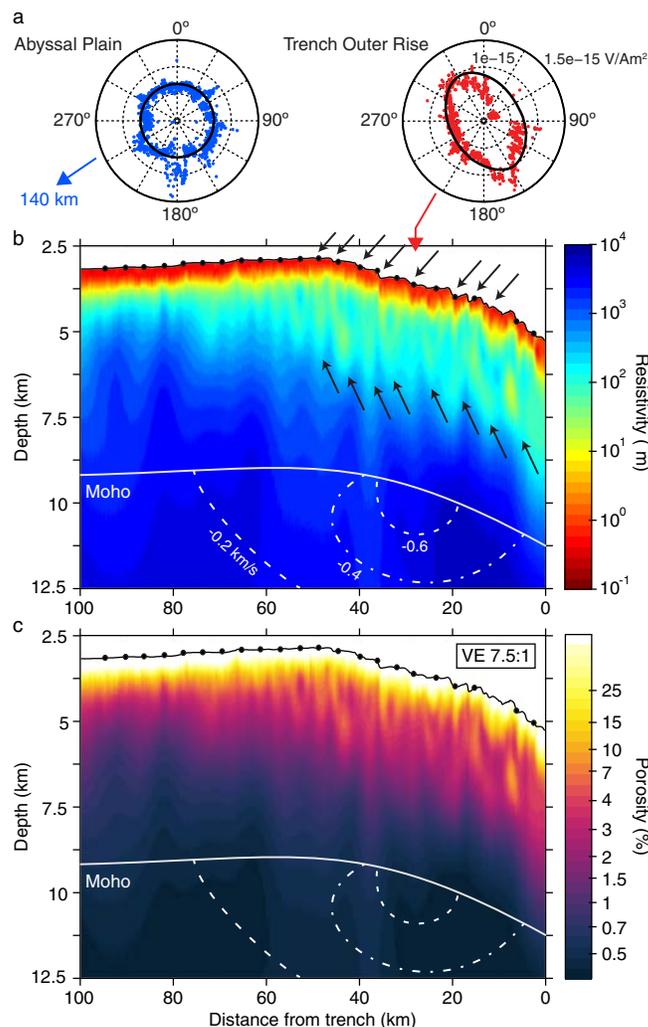
Figure 5. Close-up of outer rise electrical structure. (a) LEM anisotropy circles at 0.75 Hz, modified from *Key et al.* [2012]. The abyssal plain LEM, deployed 140 km from the trench axis, detects isotropic basement. In contrast, the trench-outer rise LEM shows significant anisotropy that is aligned parallel with the bending fault fabric. (b) The seafloor shows predominantly layered 1-D resistivity structure seaward of 60 km from the trench, at which point subvertical conductive channels begin to develop. The low resistivity channels are associated with fault scarps and require significant crustal hydration. The black filled circles show EM receiver locations, the white solid line is the Moho, and the white dashed lines show contours of seismic P-wave velocity reductions interpreted to be serpentinized mantle [*Ivandic et al.*, 2008]. (c) Porosity estimated from the resistivity with Archie's law.

A previous 1-D analysis of the CSEM data was performed by *Key et al.* [2012] and the results are mostly consistent with those presented here. Figure 3 shows our 2-D model responses for an abyssal plain as well as a trench-outer rise site. A qualitative comparison with the 1-D responses shown in *Key et al.* [2012] highlights the significantly better data fits in 2-D, particularly near rugged seafloor relief associated with faulting. Note that our 2-D model responses fit the data to a 2% error floor whereas the 1-D results were fit to a 15% error floor. In contrast to 2-D, the 1-D model responses are unable to capture the data trends for both amplitude and phase in the vicinity of fault scarps. This is partly due to the fact that the 1-D discretization does not incorporate bathymetry, which is necessary to accurately calculate forward model responses. More importantly, 1-D models are horizontally layered while our data require lateral heterogeneity, which is readily distinguished above fault scarps in Figure 3. This is further demonstrated by our 2-D inversion model result, which shows lateral resistivity variations with scale lengths much shorter than the spacing between seafloor receivers (e.g., 1–3 km wide conductive channels versus 4–10 km receiver separations). The marked improvement in spatial resolution from 2-D modeling is possible since the effective transmitter spacing for our inverted data set is approximately 100 m, which allows us to image new resistivity features not seen in the stitched 1-D results, including subvertical conductive fault channels and variations in the thickness of seafloor sediments. Furthermore, we are able to better constrain the resistivity of the uppermost mantle.

We are unlikely to see improvements to the 2-D data fits with 3-D modeling since the 2% error floor represents the navigational error. Additionally, we consider 2-D modeling sufficient because the survey transect is aligned perpendicular to the bathymetry and tectonic fabric. The electrical anisotropy seen by *Key et al.* [2012] is also perpendicular to the transect and reiterates the data compatibility with 2-D methods.

3.3. Data Resolution and Sensitivity
In order to investigate the sensitivity of CSEM data to subvertical conductive channels coincident with fault scarps at the outer rise, we construct two synthetic resistivity models that contain the same bathymetry and
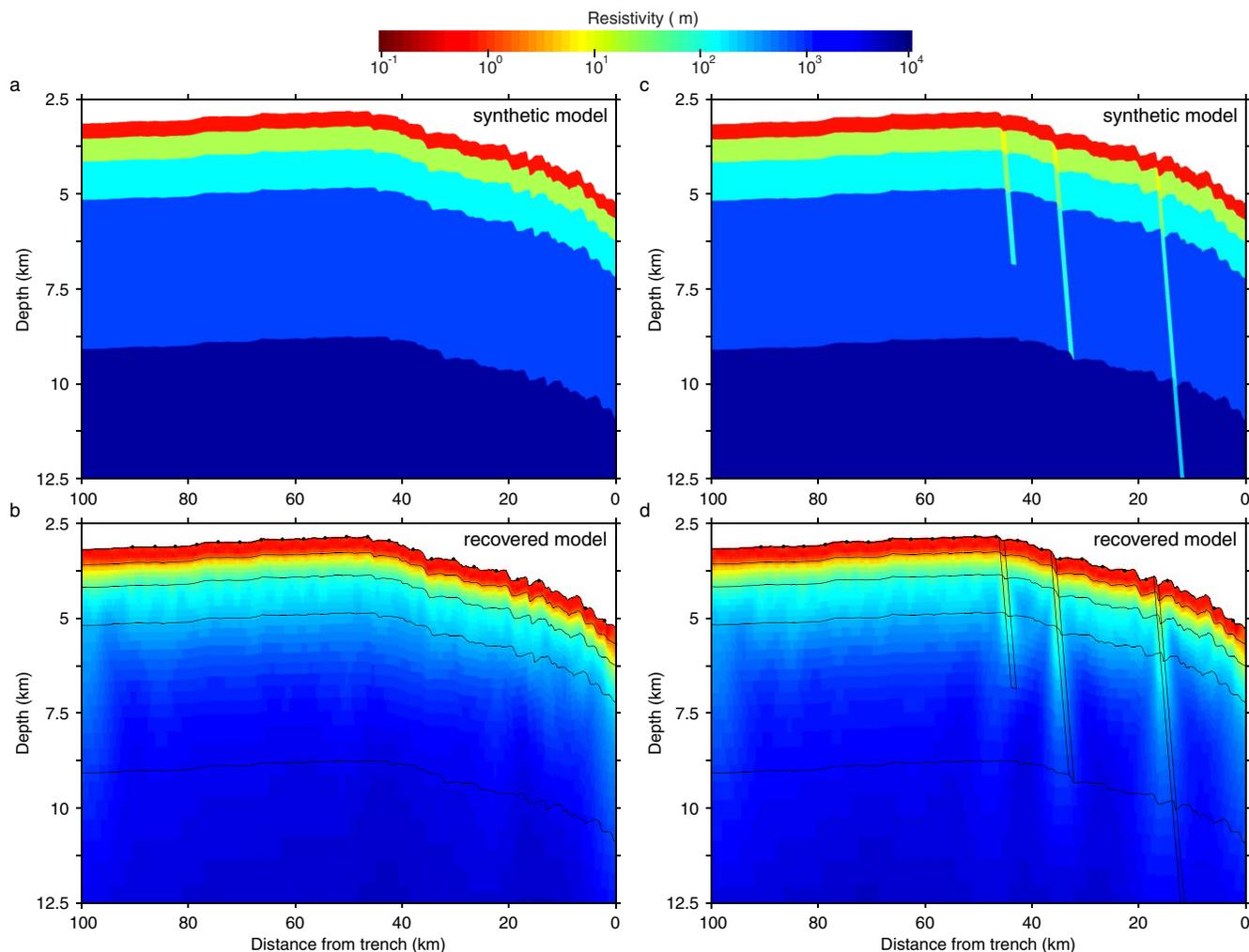
Figure 6. Synthetic model studies. (a) Layered forward model with no faults. (b) Inversion of the synthetic data from no fault model. (c) Layered forward model with faults. (d) Inversion of the synthetic data from fault model.

data density as our inverted data set. Figure 6a shows a simple 1-D layered half-space model with no conductive channels. The layer depths and resistivities are prescribed to reflect the expected porosity of 400 m of sediment underlain by 24 Ma oceanic crust. The second model, shown in Figure 6c, adds three conductive channels that represent fault damage zones (FDZ) having enhanced porosity. The channels dip 60° clockwise from horizontal and penetrate the upper crust, the lower crust, and the upper mantle, respectively. The channels are approximately 1 km wide and are placed 15 km, 35 km, and 45 km seaward of the trench. We calculate forward CSEM responses for the synthetic models, add 2% random noise, and then invert the resulting synthetic data. The two synthetic data inversions converge to a final RMS of 1.0. The final converged resistivity models in Figures 6b and 6d show that the CSEM data are sensitive to the presence of conductive channels to upper mantle depths, but the resolution progressively diminishes below midcrustal depths.

The impact of a conductive channel on the CSEM data will diminish as the channel width is reduced. We vary the width of the conductive channels in the synthetic model shown in Figure 6c and find that the channels must be at least 200 m wide for the data to deviate beyond the 2% error floor. Note that this lower bound limit is specific to the data density used in our inverted data set.

Although the width of a fault gouge zone is on a submeter scale, the FDZ—arising from deformation due to strain localization—is thought to be hundreds of meters to a few kilometers wide [*Cochran et al.*, 2009].

Since both permeability and porosity are likely enhanced within the FDZ, our results suggest that trench-outer rise bending faults have damage zones on the order of 1–2 km wide.

However, CSEM data are highly sensitive to the conductivity-thickness product. At the limit of the data resolution, thinner more conductive channels are difficult to distinguish from wider less conductive channels. We used the Occam algorithm to invert for resistivity, which searches for the smoothest possible model that fits the data to an RMS of 1.0 [*de Groot-Hedlin and Constable*, 1990]. Hence, the channel widths observed in Figure 5b are upper bounds; the true in situ widths may be sharper and more conductive. The tradeoff is that a more conductive channel requires larger porosity.

4. Hydration of Faulted Oceanic Crust

4.1. Porosity Estimates and Uncertainties

While our CSEM inversion demonstrates that electrical resistivity can qualitatively map fluid pathways and fault damage zones, we must quantify porosity to constrain the volume of pore fluid in the crust. We apply Archie's law, a robust empirical relationship [*Archie*, 1942], to estimate bulk porosity from our electrical resistivity model

$$\phi = \left(\frac{\rho_w}{\rho}\right)^{1/m} \tag{1}$$

where ρ is the bulk resistivity, ρ_w is the pore fluid resistivity, ϕ is the porosity, and m is the cementation exponent.

Since the resistivity of saline fluid varies as a function of temperature [*Quist and Marshall*, 1968], we apply the model of *Constable et al.* [2009] to estimate the pore fluid resistivity:

$$\rho_w(T) = \left[2.903916\left(1 + 2.97175 \times 10^{-2}T + 1.5551 \times 10^{-4}T^2 - 6.7 \times 10^{-7}T^3\right)\right]^{-1} \tag{2}$$

where T is temperature in degrees Celsius. We prescribe the temperature for the 24 Ma crust using the *Hasterok* [2013] plate cooling model. However, anomalously low heat flux observed on the Cocos plate offshore of Nicaragua indicates vigorous hydrothermal circulation in the extrusive crust that advects heat and cools the lithosphere [*Fisher et al.*, 2003a; *Grevemeyer et al.*, 2005; *Hutnak et al.*, 2007]. Conservatively prescribing temperature with a plate cooling model ignores the effect of hydrothermal circulation. The warmer geotherm will underestimate pore fluid resistivity and as a consequence underestimate bulk porosity. Hence, we also use a colder geotherm suitable for well-ventilated crust with 10 mW/m^2 heat flux. We follow the example used in *Harris et al.* [2010] and construct a geotherm with a 10°C/km gradient in the sediment, an isothermal extrusive layer, and a 30°C/km gradient below. In addition to temperature, bulk resistivity is sensitive to the degree to which pores are interconnected, which is incorporated into the cementation exponent in Archie's law. We assign a cementation exponent of $m = 2$ based on constraints from laboratory and in situ seafloor logging measurements of the Cocos crust [*Brace and Orange*, 1968; *Becker et al.*, 1982; *Becker*, 1985]. The resulting porosity cross section is shown in Figure 5c.

Basement temperatures may be spatially heterogenous, in which case the application of a 1-D geotherm would introduce errors in our porosity estimates. Away from regions showing anomalous heat flow, lateral temperature variations are a second-order effect relative to the dominant depth-dependent gradient. Crustal temperatures must be increased by well over 100°C to explain our observed resistivity variations. Such a large increase in basement temperature is highly unlikely as it is inconsistent with heat flux measurements across bending faults on the EPR-Cocos seafloor [*Hutnak et al.*, 2007]. Thus, a 1-D geotherm is sufficient.

In contrast, lateral cementation exponent variations may have a moderate impact on our porosity estimates. The scale and magnitude of variations in the bulk permeability structure of faulted seafloor are poorly constrained. Nonetheless, the cementation exponent must be reduced to less than $m = 1.5$ throughout the intrusive crust to accommodate the resistivity reductions we observe within 60 km of the trench. A large decrease in the cementation exponent reflects significantly enhanced permeabilities [*Wong et al.*, 1984], which would drive widespread heat advection via hydrothermal circulation [*Iyer et al.*, 2012]. This is also inconsistent with nearby heat flux measurements [*Hutnak et al.*, 2007]. The most probable scenario in
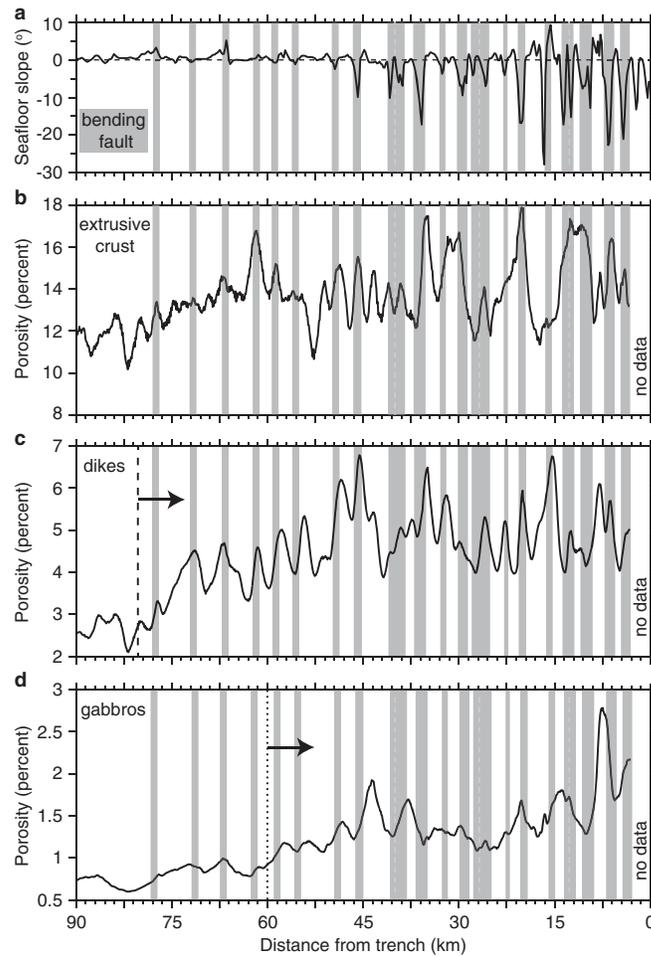
Figure 7. Faults correlate with enhanced crustal porosity. (a) The bathymetric slope of the seafloor along our survey transect clearly identifies the location of faults, which express suddenly steepened gradients. The vertically averaged porosity of the (b) extrusive, (c) dike, and (d) gabbro crustal layers. We highlight the location and width of fault zones at the seafloor as gray shaded regions, and shift them laterally to mark their respective location at depth assuming a 60° dipping fault. The slight offsets between the seafloor fault location and the peak porosity at depth reflects the dip of the faults, which is in good agreement with the shaded regions.

faulted oceanic crust is some combination of enhanced porosity, enhanced permeability, and cooler temperatures. Thus, without additional constraints on the cementation exponent, our porosity estimates provide an upper bound.

4.2. Porosity of Crustal Layers

We can gain better insight into the relationship between porosity and bending faults by inspecting the lateral variability within each crustal layer. Oceanic crust typically contains three lithologically distinct layers of extrusive volcanics (layers 2a and 2b), sheeted diabase dikes (layer 2c), and plutonic gabbros (layer 3) that each exhibit contrasting porosities. The average oceanic crust is 7.1 km thick, with 2.1 km layer 2 and 5 km layer 3 thicknesses [*White et al.*, 1992]. The Cocos crust extrusive layer was found to be 600 m thick in ODP Hole 504B [*Becker et al.*, 1989]. Seismic reflection data off Nicaragua detect a 5.5 km thick crust consisting of 1.5 km layer 2 and 4 km layer 3 thicknesses [*Walther et al.*, 2000; *Ivandic et al.*, 2008]. Thus, we assume the Cocos crust contains 600 m of extrusives, 1 km of dikes, and 4 km of gabbros. Since the sediment cover varies in thickness along our transect, we define the depth to the top of the basement with a 3.5 Ωm contour, equivalent to approximately 20% porosity.

We remove the sediment cover and separate the porosity into three sections that correspond to the extrusive, dike and gabbro layers. Figure 7a shows the bathymetric slope angle along our transect, which we use
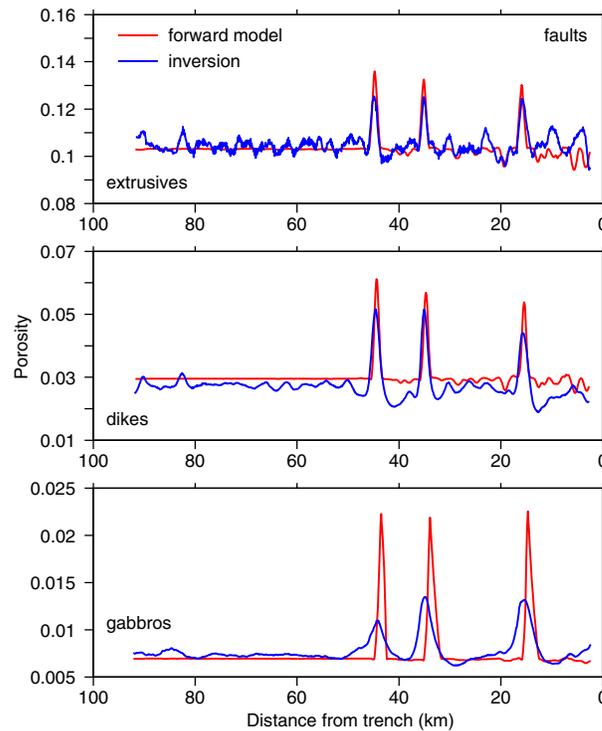
Figure 8. Porosity estimates for the pair of synthetic fault models shown in Figures 6c–6d. The red line is the porosity of the forward model and the blue line is the porosity of the synthetic inversion model. The forward and inverse model porosities show good agreement. The inversion loses resolution in the gabbros, but the integrated porosities are conserved.

to identify the location of steep seafloor faults. Figures 7b–7d shows the vertically averaged porosity—estimated with the more representative colder geotherm—for each layer. Taken together, we see that faulted regions correlate with zones of enhanced porosity. The porous fault zones are typically 1–2 km, 2–3 km, and 3–5 km wide in the layer of extrusives, dikes, and gabbros, respectively. We find that the onset of crustal hydration begins 80 km and 60 km seaward of the trench in the layer of dikes and gabbros, respectively.

The apparently larger channel widths in the lower crust are likely due to progressively decreasing model resolution as a function of depth. The porous fault zone width estimates are upper bounds; the true in situ widths of enhanced porosity may be sharper and more conductive. Since our data are sensitive to the conductivity-thickness product, reducing the width of a channel requires increasing the conductivity by an equal factor. For a constant cementation exponent, a more conductive channel requires a larger porosity.

We use the synthetic examples in Figure 6 to test the robustness of our porosity estimates. We calculate porosity from the forward and inverse models with the same procedure outlined above. After removing the layer of sediment, we vertically average the porosity along track for each crustal layer. Figure 8 compares the porosities estimated from the forward model with those estimated from the inverse model. The results show that we do a good job of recovering the conductive fault channels in all three crustal layers, but lose some resolution in the deeper gabbro layer. Although we lose resolution in the gabbros, the integrated porosities are almost identical for the starting and inverted models, averaging 0.7% and 0.75% in an unfaulted segment and 0.89% and 0.9% in a faulted segment, respectively.

In light of the data sensitivity to the conductivity-thickness product, the laterally averaged porosity for a segment of the seafloor containing multiple faults is less sensitive to the true channel widths. Thus, laterally averaged porosity is less sensitive to the data resolution and our choice of regularization as well. We divide the porosity cross section into 20 km wide windows beginning at the trench and extending 100 km seaward. Then, for each window, we laterally average the porosity to show its trend as a function of depth. The five curves are plotted alongside averaged resistivity in Figure 9. The window furthest from the trench (80–100 km) represents normal oceanic lithosphere with no signs of faulting in the bathymetry and each successive window features a rising intensity of faulting as expressed on the seafloor. Figure 9 shows progressively less resistive and more porous crust with proximity to the trench that correlates with increasing fault density and fault throw, consistent with the trend seen in Figure 7.

Table 1 reports the average porosity of each crustal layer in 20 km intervals. The low heat flux measurements demonstrate that the EPR-Cocos extrusive crust is both colder and more permeable than typical oceanic crust. Higher permeability may reflect a lower cementation exponent [*Walsh and Brace*, 1984]. Matters are further complicated by surface charge conduction in clay minerals. Since clay is a prominent secondary mineral in the upper crust, ignoring its contribution to conduction yields overestimated porosity [*Pezard*, 1990; *Evans*, 1994]. We acknowledge these uncertainties and elect to simply use an Archie's exponent of $m = 1.6$ as a lower bound for the extrusive crust.
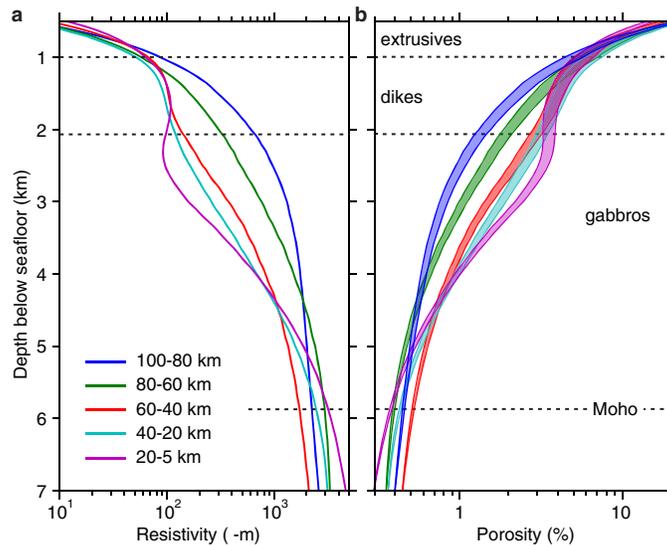
Figure 9. Broad-scale increase of crustal porosity with proximity to the trench. (a) Lines show the averaged bulk resistivity as a function of depth of five 20 km wide sections from the trench to 100 km seaward. (b) Porosity estimated from the averaged resistivity sections of Figure 9a using Archie's law with a cementation exponent of $m = 2$. Lower bound estimates are based on temperatures from the warmer plate cooling thermal model [*Hasterok*, 2013] and upper bound from a colder thermal model that considers hydrothermal circulation [*Harris et al.*, 2010].

The crustal porosity and the density of conductive faults progressively increase with proximity to the trench. The extrusive crust is only slightly affected by faulting since its porosity increases by a factor of 1.2 as the Cocos plate traverses the outer rise. Conversely, the porosity of the intrusive crust is considerably enhanced by faulting, increasing by a factor of 1.8 and 2.5 in the sheeted dikes and gabbros, respectively. We conclude that bending faults effectively double the pore water content of the intrusive crust.

Alternatively, we can average resistivity first and then proceed to calculate porosity, which results in slightly smaller estimates (Table 1). While the differences are minimal, we prefer to perform averaging on the porosity. The depth to the top of the basement varies along the survey transect. By averaging resistivity first, we lose information on the changing basement depth. Since an uplifted fault scarp is prone to erosion, there is less sediment above the scarp and more sediment on the hanging wall. Thus, we cannot apply pore fluid temperature consistently to calculate porosity if the resistivity is averaged over an area with significantly varying sediment thickness. The porosity calculations are biased downward where there is less sediment on average and upward where there is more sediment on average. The procedural bias is small relative to uncertainties stemming from temperature and cementation variations along strike, which we are unable to account for. Ultimately, the uncertainties are important when considering the absolute magnitude of the porosity, but not the substantial changes we observe relative to the abyssal plain.

The expected porosity for 24 Ma oceanic crust—from the in-depth analysis of *Jarrard* [2003]—is in good agreement with the porosities from the seaward end of our transect and corroborate the significant enhancement we observe at the trench-outer rise. The total porosity integrated over a hypothetical 7.1 km thick 24 Ma "normal" oceanic crust is equivalent to a 140 m column of water, which agrees well with the 125 m we estimate in the 5.5 km crust at the seaward end of our transect. After having undergone faulting at the outer rise, the Cocos crust transports a 200 m layer of water into the trench, an increase of over 40% compared with "normal" crust.

5. Discussion

The addition of water to unaltered basaltic crust will inevitably lead to alteration and hydrous mineral formation [*Staudigel*, 2014]. We have shown that the average crustal porosity progressively grows until it peaks at the trench, whereby hydration likely persists for as

Table 1. Percent Porosity of the Incoming Oceanic Crust

Segment	Extrusives	Dikes	Gabbros
distance from trench	$m=1.6, \ 2$	$m=2$	$m=2$
24 Ma crust[a]	10.4	3.0	0.7
$\rho \ \rightarrow \ \phi \ \rightarrow \text{mean}(\phi)$[b]			
80–100 km	7.5, 12.2	2.7	0.7
60–80 km	8.5, 13.5	3.7	0.8
40–60 km	8.5, 13.5	4.7	1.3
20–40 km	8.9, 14.1	4.8	1.3
5–20 km	9.1, 14.3	4.8	1.7
$\rho \ \rightarrow \ \text{mean}(\rho) \rightarrow \text{mean}(\phi)$[c]			
80–100 km	7.2, 11.9	2.6	0.7
60–80 km	8.1, 13.1	3.6	0.8
40–60 km	8.1, 13.1	4.5	1.2
20–40 km	8.4, 13.5	4.7	1.3
5–20 km	8.5, 13.6	4.5	1.5

[a]From *Jarrard* [2003].
[b]Average porosity from porosity cross section.
[c]Average porosity from average resistivity.

long as the plate traverses the outer rise. The enhanced porosities are concentrated along fault trajectories, which indicates that hydration is localized. The localized hydration seen here suggests the development of a heterogeneous pattern of crustal alteration. This likely impacts both the timing and the magnitude of dewatering from metamorphic dehydration reactions during subduction, significantly increasing the flux of water beneath the fore arc and arc while reducing the flux to the deeper postarc mantle [*Wada et al.*, 2012].

Although we image resistivity reductions in the outer rise crust, we do not detect reduced resistivity in the upper mantle. Indeed, there is a slight increase in resistivity in the mantle beneath the outer rise, which is consistent with a feature in our previously published MT data [*Naif et al.*, 2013]. The resistive mantle in our model suggests that fracture porosity is not noticeably increased by bending faults. Serpentinites can host large quantities of magnetite [*Frost*, 1985; *O'Hanley and Dyar*, 1993] and as such may be resistive or conductive depending on whether or not interconnected magnetite veins are formed as reaction byproducts [*Stesky and Brace*, 1973; *Reynard et al.*, 2011].

Assuming that the mantle undergoes serpentinization at low porosity conditions in the outer rise, the high mantle resistivity rules out magnetite vein formation. A lack of magnetite suggests that the upper mantle at the outer rise is a closed low fluid flux system [*Bach et al.*, 2006] that is unlikely to reach 40% serpentinization [*Andreani et al.*, 2007]. Since bending faults have been imaged to extend to mantle depths [*Ranero et al.*, 2003], we would expect the triggering of serpentinization reactions to consume pore water and reduce porosity by the ensuing volumetric expansion [*Moody*, 1976]. Thus, in the absence of magnetite veins, a lack of reduced mantle resistivity at the outer rise is not incompatible with serpentinization, and the small increase in resistivity may, perhaps, suggest it.

Serpentinization is a highly exothermic chemical reaction, releasing nearly 300 kJ/kg of heat [*Macdonald and Fyfe*, 1985]. Thermal data from the EPR-Cocos crust detect elevated heat flux values above bending faults. In contrast to seismic observations, the thermal data can be simply explained with conductive numerical models without requiring serpentinization [*Hutnak et al.*, 2007]. However, if outer rise serpentinization is a closed system where a low flux of water is transported by downward percolation, its thermal expression on the seafloor may be limited [*Emmanuel and Berkowitz*, 2006; *Iyer et al.*, 2012]. Additionally, vigorous open-cell circulation in the extrusive crust possibly masks its thermal signature.

The sum of the electrical, thermal, and seismic observations on the EPR-Cocos crust lead us to conclude that mantle serpentinization operates in a closed system with low fluid fluxes and low porosities. Since serpentinization induces fracturing in order to accommodate volumetric expansion [*O'Hanley*, 1992], we propose that reaction-driven fracturing controls the kinetics of outer rise serpentinization beyond the bending fault related onset.

Regardless of the potential for hydration in the upper mantle, our observations clearly show that bending faults significantly hydrate the crust. The water-rich oceanic crust that we observe at the outer rise is consistent with seismic data that detect a highly hydrous subducted crust beneath the Nicaraguan arc [*Abers et al.*, 2003] and a highly hydrous mantle wedge fed by the slab [*Syracuse et al.*, 2008; *Dinc et al.*, 2011], all of which are linked to geochemical evidence of abundant fluids at the arc itself [*Patino et al.*, 2000].

In light of our results, oceanic plates in regions displaying exposed bending faults likely contain more crustal water than originally thought. A significant fraction of the total length of convergent margins showcase numerous fault scarps at the trench-outer rise [*Masson*, 1991; *Massell*, 2002]. This suggests that both crust and sediment derived input fluxes are highly variable from margin to margin, and not only the latter. Thus, we conclude that the cumulative global magnitude of crustal water entering subduction zones exceeds existing estimates.

6. Conclusions

We used marine CSEM data collected across the trench-outer rise offshore of Nicaragua to invert for the electrical resistivity of the Cocos oceanic crust and upper mantle with 2-D numerical tools. Our final converged model fits the data to a RMS misfit of 1.0 for a 2% error floor, a significant improvement compared with previous 1-D results that fit to a 15% error floor [*Key et al.*, 2012]. The final converged model displays simple 1-D layered resistivity structure beyond 80 km seaward of the trench, which then becomes increasingly heterogenous and less resistive with proximity to the trench. The trend of decreasing resistivity is

coupled with the development of subvertical conductive channels that are collocated with bending faults at the outer rise. The conductive channels provide the first observational evidence of outer rise bending faults behaving as fluid pathways.

Our porosity estimates show that the Cocos oceanic crust is significantly enriched in pore water. Prior to faulting, the extrusive, dike, and gabbro crustal layers are 12.2%, 2.7%, and 0.7% porosity, in good agreement with independent constraints [*Jarrard*, 2003]. Within 20 km of the trench, the porosities peak at 14.3%, 4.8%, and 1.7%, respectively. Equivalently, the total crustal pore H_2O increases from a 125 m to a 200 m thick column of water, or a 60% increase. This suggests significantly more pore water is subducted with the crust than previously thought. In contrast, the upper mantle remains resistive, which suggests a low degree of serpentinization ($<$20%) that forms in a closed, low fluid flux and low porosity environment [*Bach et al.*, 2006]. Otherwise magnetite is likely to precipitate along alteration veins, producing a conductive anomaly that is not required in our data.

Fluidized bending faults—in conjunction with cold crustal temperatures, a highly permeable crustal aquifer, and hydrous alteration of the lower crust and upper mantle—have important implications for fluid cycling and the state of the Nicaraguan seismogenic zone [*Spinelli et al.*, 2006; *Spinelli and Wang*, 2008; *Saffer and Tobin*, 2011]. We speculate that faulted outer rise crust may provide optimal conditions to harbor microbial colonies at the deepest limit of life in the subseafloor biosphere, facilitated by colder crustal temperatures and sustained by potentially abundant nutrient-rich byproducts from mafic/ultramafic hydration reactions [*Takai et al.*, 2014]. Additionally, the heterogeneous pattern of hydration combined with an increased volume of subducted water may alter the flux of H_2O to the mantle wedge at arc and postarc depths [*Wada et al.*, 2012].

References

Abers, G. A., T. Plank, and B. R. Hacker (2003), The wet Nicaraguan slab, *Geophys. Res. Lett.*, *30*(2), 1098, doi:10.1029/2002GL015649.

Andreani, M., C. Mevel, A. M. Boullier, and J. Escartin (2007), Dynamic control on serpentine crystallization in veins: Constraints on hydration processes in oceanic peridotites, *Geochem. Geophys. Geosyst.*, *8*, Q02012, doi:10.1029/2006GC001373.

Archie, G. E. (1942), The electrical resistivity log as an aid in determining some reservoir characteristics, *Trans. AIME*, *146*(99), 54–62.

Baba, K., N. Tada, L. Zhang, P. Liang, H. Shimizu, and H. Utada (2013), Is the electrical conductivity of the northwestern Pacific upper mantle normal?, *Geochem. Geophys. Geosyst.*, *14*, 4969–4979, doi:10.1002/2013GC004997.

Bach, W., H. Paulick, C. J. Garrido, B. Ildefonse, W. P. Meurer, and S. E. Humphris (2006), Unraveling the sequence of serpentinization reactions: Petrography, mineral chemistry, and petrophysics of serpentinites from MAR 15°N (ODP Leg 209, Site 1274), *Geophys. Res. Lett.*, *33*, L13306, doi:10.1029/2006GL025681.

Barckhausen, U., C. R. Ranero, R. von Huene, S. C. Cande, and H. A. Roeser (2001), Revised tectonic boundaries in the Cocos Plate off Costa Rica: Implications for the segmentation of the convergent margin and for plate tectonic models, *J. Geophys. Res.*, *106*(B9), 19,207–19,220.

Becker, K. (1985), 24. Large-scale electrical resistivity and bulk porosity of the oceanic crust, Deep Sea Drilling Project Hole 504B, Costa Rica Rift, in *Initial Reports of the Deep Sea Drilling Project*, vol. 83, edited by R. N. Anderson, J. Honnorez and K. Becker, pp. 419–427, U.S. Gov. Print. Off., Washington, D. C.

Becker, K., et al. (1982), In situ electrical resistivity and bulk porosity of the oceanic crust Costa Rica Rift, *Nature*, *300*(5893), 594–598.

Becker, K., et al. (1989), Drilling deep into young oceanic crust, Hole 504B, Costa Rica Rift, *Rev. Geophys.*, *27*(1), 79–102.

Beroza, G. C., and S. Ide (2011), Slow Earthquakes and Nonvolcanic Tremor, *Annu. Rev. Earth Planet. Sci.*, *39*(1), 271–296.

Brace, W. F., and A. S. Orange (1968), Electrical resistivity changes in saturated rocks during fracture and frictional sliding, *J. Geophys. Res.*, *73*(4), 1433–1445.

Carlson, R. L., and C. N. Herrick (1990), Densities and porosities in the oceanic crust and their variations with depth and age, *J. Geophys. Res.*, *95*(B6), 9153–9170.

Carlson, R. L., and D. J. Miller (2003), Mantle wedge water contents estimated from seismic velocities in partially serpentinized peridotites, *Geophys. Res. Lett.*, *30*(5), 1250, doi:10.1029/2002GL016600.

Cochran, E. S., Y. G. Li, P. M. Shearer, S. Barbot, Y. Fialko, and J. E. Vidale (2009), Seismic and geodetic evidence for extensive, long-lived fault damage zones, *Geology*, *37*(4), 315–318.

Constable, S. (2013), Review paper: Instrumentation for marine magnetotelluric and controlled source electromagnetic sounding, *Geophys. Prospect.*, *61*(s1), 505–532.

Constable, S., and C. S. Cox (1996), Marine controlled-source electromagnetic sounding 2. The PEGASUS experiment, *J. Geophys. Res.*, *101*(B3), 5519–5530.

Constable, S., K. Key and L. Lewis (2009), Mapping offshore sedimentary structure using electromagnetic methods and terrain effects in marine magnetotelluric data, *Geophys. J. Int.*, *176*(2), 431–442.

Contreras-Reyes, E., I. Grevemeyer, E. R. Flueh, M. Scherwath, and M. Heesemann (2007), Alteration of the subducting oceanic lithosphere at the southern central Chile trench-outer rise, *Geochem. Geophys. Geosyst.*, *8*, Q07003, doi:10.1029/2007GC001632.

Cox, C. S., S. C. Constable, A. D. Chave, and S. C. Webb (1986), Controlled-source electromagnetic sounding of the oceanic lithosphere, *Nature*, *320*(6057), 52–54.

de Groot-Hedlin, C. D., and S. C. Constable (1990), Occam's inversion to generate smooth, two-dimensional models from magnetotelluric data, *Geophysics*, *55*(12), 1613–1624.

DeMets, C., R. G. Gordon, and D. F. Argus (2010), Geologically current plate motions, *Geophys. J. Int.*, *181*(1), 1–80.

Dinc, A. N., W. Rabbel, E. R. Flueh, and W. Taylor (2011), Mantle wedge hydration in Nicaragua from local earthquake tomography, *Geophys. J. Int.*, *186*(1), 99–112.

Emmanuel, S., and B. Berkowitz (2006), Suppression and stimulation of seafloor hydrothermal convection by exothermic mineral hydration, *Earth Planet. Sci. Lett.*, *243*(3-4), 657–668.

Evans, R. L. (1994), Constraints on the large-scale porosity and permeability structure of young oceanic crust from velocity and resistivity data, *Geophys. J. Int.*, *119*(3), 869–879.

Evans, R. L., M. C. Sinha, S. C. Constable and M. J. Unsworth (1994), On the electrical nature of the axial melt zone at 13° N on the East Pacific Rise, *J. Geophys. Res.*, *99*(B1), 577–588.

Faccenda, M., T. V. Gerya, and L. Burlini (2009), Deep slab hydration induced by bending-related variations in tectonic pressure, *Nat. Geosci.*, *2*(11), 790–793.

Fisher, A. T., C. A. Stein, R. N. Harris, K. Wang, E. A. Silver, M. Pfender, M. Hutnak, A. Cherkaoui, R. Bodzin, and H. Villinger (2003a), Abrupt thermal transition reveals hydrothermal boundary and role of seamounts within the Cocos Plate, *Geophys. Res. Lett.*, *30*(11), 1550, doi: 10.1029/2002GL016766.

Fisher, A. T., et al. (2003b), Hydrothermal recharge and discharge across 50 km guided by seamounts on a young ridge flank, *Nature*, *421*(6923), 618–621.

Frost, B. R. (1985), On the stability of sulfides, oxides, and native metals in serpentinite, *J. Petrol.*, *26*(1), 31–63.

Gaetani, G. A., and T. L. Grove (1998), The influence of water on melting of mantle peridotite, *Contrib. Mineral. Petrol.*, *131*(4), 323–346.

Garcia, E. S., D. T. Sandwell, and K. M. Luttrell (2015), An iterative spectral solution method for thin elastic plate flexure with variable rigidity, *Geophys. J. Int.*, *200*(2), 1010–1026.

Grevemeyer, I., N. Kaul, J. L. Diaz-Naveas, H. W. Villinger, C. R. Ranero, and C. Reichert (2005), Heat flow and bending-related faulting at subduction trenches: Case studies offshore of Nicaragua and Central Chile, *Earth Planet. Sci. Lett.*, *236*(1-2), 238–248.

Hacker, B. R. (2008), H_2O subduction beyond arcs, *Geochem. Geophys. Geosyst.*, *9*, Q03001, doi:10.1029/2007GC001707.

Harris, R. N., G. Spinelli, C. R. Ranero, I. Grevemeyer, H. Villinger, and U. Barckhausen (2010), Thermal regime of the Costa Rican convergent margin: 2. Thermal models of the shallow Middle America subduction zone offshore Costa Rica, *Geochem. Geophys. Geosyst.*, *11*, Q12S29, doi:10.1029/2010GC003273.

Hasterok, D. (2013), A heat flow based cooling model for tectonic plates, *Earth Planet. Sci. Lett.*, *361*, 34–43.

Hirschmann, M. M. (2006), Water, melting, and the deep Earth H2O cycle, *Annu. Rev. Earth Planet. Sci.*, *34*, 629–653.

Hutnak, M., et al. (2007), The thermal state of 18–24 Ma upper lithosphere subducting below the Nicoya Peninsula, northern Costa Rica margin, in *The Seismogenic Zone of Subduction Thrust Faults, MARGINS Theor. Exp. Earth Sci.*, edited by T. H. Dixon and J. C. Moore, chap. 4, pp. 86–122, Columbia Univ. Press, N. Y.

Hutnak, M., A. T. Fisher, R. Harris, C. Stein, K. Wang, G. Spinelli, M. Schindler, H. Villinger, and E. Silver (2008), Large heat and fluid fluxes driven through mid-plate outcrops on ocean crust, *Nat. Geosci.*, *1*(9), 611–614.

Ivandic, M., I. Grevemeyer, A. Berhorst, E. R. Flueh, and K. McIntosh (2008), Impact of bending related faulting on the seismic properties of the incoming oceanic plate offshore of Nicaragua, *J. Geophys. Res.*, *113*, B05410, doi:10.1029/2007JB005291.

Ivandic, M., I. Grevemeyer, J. Bialas, and C. J. Petersen (2010), Serpentinization in the trench-outer rise region offshore of Nicaragua: Constraints from seismic refraction and wide-angle data, *Geophys. J. Int.*, *180*(3), 1253–1264.

Iyer, K., L. H. Rüpke, J. P. Morgan, and I. Grevemeyer (2012), Controls of faulting and reaction kinetics on serpentinization and double Beni-off zones, *Geochem. Geophys. Geosyst.*, *13*, Q09010, doi:10.1029/2012GC004304.

Jarrard, R. D. (2003), Subduction fluxes of water, carbon dioxide, chlorine, and potassium, *Geochem. Geophys. Geosyst.*, *4*(5), 8905, doi: 10.1029/2002GC000392.

Kaproth, B. M., and C. Marone (2013), Slow earthquakes, preseismic velocity changes, and the origin of slow frictional stick-slip, *Science*, *341*(6151), 1229–1232.

Kastner, M., E. A. Solomon, R. N. Harris, and M. E. Torres (2014), Chapter 4.4.3—Fluid origins, thermal regimes, and fluid and solute fluxes in the forearc of subduction zones, in *Earth and Life Processes Discovered from Subseafloor Environments A Decade of Science Achieved by the Integrated Ocean Drilling Program (IODP), Dev. Mar. Geol.*, vol. 7, edited by R. Stein et al., pp. 671–733, Elsevier, Amsterdam, Netherlands.

Key, K. (2009), 1D inversion of multicomponent, multifrequency marine CSEM data: Methodology and synthetic studies for resolving thin resistive layers, *Geophysics*, *74*(2), F9–F20.

Key, K. (2012), Marine EM inversion using unstructured grids: A 2D parallel adaptive finite element algorithm, in *SEG Technical Program Expanded Abstracts*, no. 9, pp. 1–5, Las Vegas.

Key, K. and J. Ovall (2011), A parallel goal-oriented adaptive finite element method for 2.5-D electromagnetic modelling, *Geophys. J. Int.*, *186*(1), 137–154.

Key, K., S. Constable, T. Matsuno, R. L. Evans and D. Myer (2012), Electromagnetic detection of plate hydration due to bending faults at the Middle America Trench, *Earth Planet. Sci. Lett.*, *351*, 45–53.

Key, K., S. Constable, L. Liu, and A. Pommier (2013), Electrical image of passive mantle upwelling beneath the northern East Pacific Rise, *Nature*, *495*(7442), 499–502.

Kushiro, I., Y. Syono, and S. I. Akimoto (1968), Melting of a peridotite nodule at high pressures and high water pressures, *J. Geophys. Res.*, *73*(18), 6023–6029.

Levitt, D. A., and D. T. Sandwell (1995), Lithospheric bending at subduction zones based on depth soundings and satellite gravity, *J. Geophys. Res.*, *100*(B1), 379–400.

Macdonald, A. H., and W. S. Fyfe (1985), Rate of serpentinization in seafloor environments, *Tectonophysics*, *116*(1), 123–135.

Mann, P., R. D. Rogers, and L. Gahagan (2007), Overview of plate tectonic history and its unresolved tectonic problems, in *Central America: Geology, Resources and Hazards*, vol. 1, edited by J. Bundschuh and G. E. Alvarado, chap. 8, pp. 205–241, Taylor and Francis, London, U. K.

Massell, C. G. (2002), Large scale structural variation of trench outer slopes and rises, PhD thesis, Univ. of Calif., San Diego, Calif.

Masson, D. G. (1991), Fault patterns at outer trench walls, *Mar. Geophys. Res.*, *13*(3), 209–225.

Moody, J. (1976), Serpentinization: A review, *Lithos*, *9*, 125–138.

Morris, J. D., W. P. Leeman, and F. Tera (1990), The subducted component in island arc lavas: Constraints from Be isotopes and B-Be systematics, *Nature*, *344*(6261), 31–36.

Myer, D., S. Constable, and K. Key (2011), Broad-band waveforms and robust processing for marine CSEM surveys, *Geophys. J. Int.*, *184*(2), 689–698.

Naif, S., K. Key, S. Constable, and R. L. Evans (2013), Melt-rich channel observed at the lithosphere–asthenosphere boundary, *Nature*, *495*(7441), 356–359.

O'Hanley, D. S. (1992), Solution to the volume problem in serpentinization, *Geology*, *20*(8), 705–708.

O'Hanley, D. S., and M. D. Dyar (1993), The composition of lizardite 1t and the formation of magnetite in serpentinites, *Am. Mineral.*, *78*(3-4), 391–404.

Patino, L. C., M. J. Carr, and M. D. Feigenson (2000), Local and regional variations in Central American arc lavas controlled by variations in subducted sediment input, *Contrib. Mineral. Petrol.*, *138*(3), 265–283.

Peacock, S. M. (2001), Are the lower planes of double seismic zones caused by serpentine dehydration in subducting oceanic mantle?, *Geology*, *29*(4), 299–302.

Pezard, P. A. (1990), Electrical properties of mid-ocean ridge basalt and implications for the structure of the upper oceanic crust in Hole 504B, *J. Geophys. Res.*, *95*(B6), 9237–9264.

Plank, T., and C. H. Langmuir (1998), The chemical composition of subducting sediment and its consequences for the crust and mantle, *Chem. Geol.*, *145*(3-4), 325–394.

Plank, T., V. Balzer, and M. Carr (2002), Nicaraguan volcanoes record paleoceanographic changes accompanying closure of the Panama gateway, *Geology*, *30*(12), 1087–1090.

Quist, A. S., and W. L. Marshall (1968), Electrical conductances of aqueous sodium chloride solutions from 0 to 800 degree and at pressures to 4000 bars, *J. Phys. Chem.*, *72*(2), 684–703.

Ranero, C. R., and V. Sallarès (2004), Geophysical evidence for hydration of the crust and mantle of the Nazca plate during bending at the north Chile trench, *Geology*, *32*(7), 549–552.

Ranero, C. R., J. Phipps Morgan, K. McIntosh, and C. Reichert (2003), Bending-related faulting and mantle serpentinization at the Middle America trench, *Nature*, *425*(6956), 367–373.

Reynard, B., K. Mibe, and B. Van de Moortèle (2011), Electrical conductivity of the serpentinised mantle and fluid flow in subduction zones, *Earth Planet. Sci. Lett.*, *307*(3-4), 387–394.

Rüpke, L. H., J. P. Morgan, M. Hort, and J. A. D. Connolly (2002), Are the regional variations in Central American arc lavas due to differing basaltic versus peridotitic slab sources of fluids?, *Geology*, *30*(11), 1035.

Rüpke, L. H., J. P. Morgan, M. Hort, and J. A. D. Connolly (2004), Serpentine and the subduction zone water cycle, *Earth Planet. Sci. Lett.*, *223*, 17–34.

Rychert, C. A., K. M. Fischer, G. A. Abers, T. Plank, E. Syracuse, J. M. Protti, V. Gonzalez, and W. Strauch (2008), Strong along-arc variations in attenuation in the mantle wedge beneath Costa Rica and Nicaragua, *Geochem. Geophys. Geosyst.*, *9*, Q10S10, doi:10.1029/2008GC002040.

Saffer, D. M., and H. J. Tobin (2011), Hydrogeology and mechanics of subduction zone forearcs: Fluid flow and pore pressure, *Annu. Rev. Earth Planet. Sci.*, *39*(1), 157–186.

Scholz, C. H. (1998), Earthquakes and friction laws, *Nature*, *391*(6662), 37–42.

Spinelli, G. A., and K. Wang (2008), Effects of fluid circulation in subducting crust on Nankai margin seismogenic zone temperatures, *Geology*, *36*(11), 887–890.

Spinelli, G. A., D. M. Saffer, and M. B. Underwood (2006), Hydrogeologic responses to three-dimensional temperature variability, Costa Rica subduction margin, *J. Geophys. Res.*, *111*, B04403, doi:10.1029/2004JB003436.

Staudigel, H. (2014), 4.16 - Chemical fluxes from hydrothermal alteration of the oceanic crust, in *Treatise on Geochemistry*, edited by K. K. Turekian and H. D. Heinrich, 2 ed., pp. 583–606, Elsevier, Oxford, U. K.

Stesky, R. M., and W. F. Brace (1973), Electrical conductivity of serpentinized rocks to 6 kilobars, *J. Geophys. Res.*, *78*(32), 7614–7621.

Syracuse, E. M., G. A. Abers, K. Fischer, L. MacKenzie, C. Rychert, M. Protti, V. González, and W. Strauch (2008), Seismic tomography and earthquake locations in the Nicaraguan and Costa Rican upper mantle, *Geochem. Geophys. Geosyst.*, *9*, Q07S08, doi:10.1029/2008GC001963.

Takai, K., K. Nakamura, D. LaRowe, and J. P. Amend (2014), Chapter 2.4—Life at subseafloor extremes, in *Earth and Life Processes Discovered from Subseafloor Environments A Decade of Science Achieved by the Integrated Ocean Drilling Program (IODP)*, *Dev. Mar. Geol.*, vol. 7, edited by R. Stein et al., pp. 149–174, Elsevier, Amsterdam, Netherlands.

Thompson, A. B., and J. A. D. Connolly (1992), Migration of metamorphic fluid: Some aspects of mass and heat transfer, *Earth Sci. Rev.*, *32*(1-2), 107–121.

Ulmer, P., and V. Trommsdorff (1995), Serpentine stability to mantle depths and subduction-related magmatism, *Science*, *268*(5212), 858–861.

van Avendonk, H. J. A., W. S. Holbrook, D. Lizarralde, and P. Denyer (2011), Structure and serpentinization of the subducting Cocos plate offshore Nicaragua and Costa Rica, *Geochem. Geophys. Geosyst.*, *12*, Q06009, doi:10.1029/2011GC003592.

van Keken, P., B. R. Hacker, E. M. Syracuse and G. A. Abers (2011), Subduction factory: 4. Depth-dependent flux of H_2O from subducting slabs worldwide, *J. Geophys. Res.*, *116*, B01401, doi:10.1029/2010JB007922.

Wada, I., M. D. Behn, and A. M. Shaw (2012), Effects of heterogeneous hydration in the incoming plate, slab rehydration, and mantle wedge hydration on slab-derived H_2O flux in subduction zones, *Earth Planet. Sci. Lett.*, *353–354*, 60–71.

Walsh, J. B., and W. F. Brace (1984), The effect of pressure on porosity and the transport-properties of rock, *J. Geophys. Res.*, *89*(B11), 9425–9431.

Walther, C. H. E., E. R. Flueh, C. R. Ranero, R. von Huene, and W. Strauch (2000), Crustal structure across the Pacific margin of Nicaragua: Evidence for ophiolitic basement and a shallow mantle sliver, *Geophys. J. Int.*, *141*(3), 759–777.

Weinrebe, W., and C. R. Ranero (2012), Multibeam Bathymetry Compilation of the Central America Pacific Margin, Integrated Earth Data Applications, doi:10.1594/IEDA/100069.

White, R. S., D. McKenzie, and R. K. O'Nions (1992), Oceanic crustal thickness from seismic measurements and rare earth element inversions, *J. Geophys. Res.*, *97*(B13), 19,683–19,715.

Wong, P., J. Koplik, and J. P. Tomanic (1984), Conductivity and permeability of rocks, *Phys. Rev. B*, *30*(11), 6606–6616.

Worzewski, T., M. Jegen, H. Kopp, H. Brasse, and W. T. Castillo (2010), Magnetotelluric image of the fluid cycle in the Costa Rican subduction zone, *Nat. Geosci.*, *4*(2), 108–111.